

Metastable amorphous chromium–vanadium oxide nanoparticles with superior performance as a new lithium battery cathode

Jinzhi Sheng[§], Qidong Li[§], Qiulong Wei, Pengfei Zhang, Qinqin Wang, Fan Lv, Qinyou An, Wei Chen (✉), and Liqiang Mai (✉)

State Key Laboratory of Advanced Technology for Materials Synthesis and Processing, WUT–Harvard Joint Nano Key Laboratory, Wuhan University of Technology, Wuhan 430070, China

[§] These authors contributed equally to this work.

Received: 22 April 2014

Revised: 20 June 2014

Accepted: 21 June 2014

© Tsinghua University Press and Springer-Verlag Berlin Heidelberg 2014

KEYWORDS

$\text{Cr}_2\text{V}_4\text{O}_{13}$, nanoparticles, metastable amorphous structure, lithium battery

ABSTRACT

The main drawbacks of vanadium oxide as a cathode material are its low conductivity, low practical capacity and poor cycling stability. Adding Cr can improve its conductivity and a metastable amorphous state may provide higher capacity and stability. In this work, metastable amorphous Cr–V–O nanoparticles have been successfully prepared through a facile co-precipitation reaction followed by annealing treatment. As a cathode material for lithium batteries, the metastable amorphous Cr–V–O nanoparticles exhibit high capacity (260 mAh/g at 100 mA/g between 1.5–4 V), low capacity loss (more than 80% was retained after 200 cycles at 100 mA/g) and high rate capability (up to 3 A/g).

1 Introduction

The storage of electrical energy plays an important role in today's society. The continuous evolution of mobile and power electronics, such as cellular phones, laptops and electric vehicles, requires types of high power and high energy-density storage devices [1–7]. To meet these requirements, lithium batteries (LBs) are the preferred choice for energy storage due to

their high energy density, long cycle life and environmentally benign features [8–11]. For LBs, the energy density mainly depends on their cathodes [12–14]. However, existing commercial cathode materials only provide a relatively low specific capacity (less than 200 mAh/g) [8, 15–18]. Thus, the development of higher capacity and high rate capability LBs is urgently desired.

In recent years, vanadium oxide materials have

Address correspondence to Wei Chen, chenwei_juan@sina.com; Liqiang Mai, mlq518@whut.edu.cn

attracted extensive attention for energy storage due to their low cost, being relatively environmentally friendly and their high theoretical capacity [19–21]. However, the decreased electron conductivity and unstable phase structure during long-term cycling limit their further development [22–27]. As an element close to vanadium, chromium (Cr) may be added to increase the electronic conductivity by adjusting the vanadium-oxide tetrahedron/octahedron, which results in enhanced lithium storage performance [28–30]. Nevertheless, the improvement of cycling stability is limited, especially for deep or more lithium insertion/extraction, since the main structure is not significantly changed by doping with small quantities of Cr [31]. Also the rate capability is still not satisfactory, due to the relatively inferior diffusion channels [31]. Disordered structures are also regarded as potential candidates for a cathode material. Recently, Lee et al. demonstrated that Li^+ diffusion can be facile in disordered materials [32]. Therefore, the utilization of amorphous materials may be an effective way to avoid the collapse of the crystalline structure [33]. Since amorphous substances have rarely been studied in the electrochemical field, studies of such materials are of great scientific value.

Herein, we report the use of metastable amorphous Cr–V–O nanoparticles as a cathode for LBs. They exhibit high specific capacity (260 mAh/g at 100 mA/g), good cycling performance (80.4% capacity remains after 200 cycles at 100 mA/g) for deep discharge (1.5–4 V) and high rate capability (up to 3 A/g), which is better than the performance of crystalline $\text{Cr}_2\text{V}_4\text{O}_{13}$.

2 Experimental

2.1 Preparation of the amorphous Cr–V–O nanoparticles

Chromium(III) nitrate ($\text{Cr}(\text{NO}_3)_3 \cdot 9\text{H}_2\text{O}$) and ammonium metavanadate (NH_4VO_3) were used as starting materials. Firstly, NH_4VO_3 powder (2 mmol) was dissolved in 50 mL of de-ionized water under magnetic stirring for 30 min at 90 °C. Secondly, $\text{Cr}(\text{NO}_3)_3 \cdot 9\text{H}_2\text{O}$ (1 mmol) was dissolved in 10 mL of de-ionized water under stirring. Thirdly, the $\text{Cr}(\text{NO}_3)_3$ solution was slowly added into the NH_4VO_3 solution with continuous

stirring for another 30 min to form the precipitate. Then the precipitate was washed three times with de-ionized water and three times with pure ethanol, and dried at 80 °C for 24 h. The obtained powder was annealed in air at 450 °C at a rate of 2 °C/min for 2 h. A series of experiments were also carried out at different annealing temperatures to further explore the electrochemical mechanism.

2.2 Material characterization

X-ray diffraction (XRD) measurements were performed to obtain crystallographic information using a D8 ADVANCE X-ray diffractometer with a non-monochromated $\text{Cu K}\alpha$ X-ray source. Thermogravimetry/differential scanning calorimetry (TG/DSC) was performed using a Netzsch STA 449C simultaneous thermal analyzer at a heating rate of 10 °C/min in air. Field emission scanning electron microscopy (FESEM) images and energy dispersive X-ray spectra (EDS) were collected with a JEOL-7100F microscope. X-ray photoelectron spectroscopy (XPS) analysis was done on a VG Multilab 2000 instrument. Transmission electron microscopy (TEM) and high-resolution transmission electron microscopy (HRTEM) images were recorded by using a JEM-2100F STEM/EDS microscope. Fourier transform infrared (FTIR) absorption spectra were recorded using a 60-SXB IR spectrometer. Brunauer–Emmett–Teller (BET) surface areas were measured using a Tristar II 3020 instrument for the adsorption of nitrogen.

2.3 Measurement of electrochemical performance

The electrochemical properties were evaluated by assembly of 2016 coin cells in a glove box filled with pure argon gas. Lithium pellets were used as the anode, a 1 M solution of LiPF_6 in ethylene carbonate (EC)/dimethyl carbonate (DMC) was used as electrolyte, and the cathode electrodes were obtained with 70% metastable amorphous Cr–V–O nanoparticles active material, 20% acetylene black and 10% poly(tetrafluoroethylene) (PTFE). Galvanostatic charge/discharge cycling was studied in a potential range of 1.5–4.0 V vs. Li^+/Li with a multichannel battery testing system (LAND CT2001A). Cyclic voltammetry (CV) and AC-impedance spectra were tested with an

electrochemical workstation (Autolab PGSTAT 302N and CHI 760D).

3 Results and discussion

In order to confirm the phase transition, DSC analysis of the as-synthesized material was carried out in air (Fig. 1(a)). It is apparent that a sharp exothermic peak occurs at 534 °C, indicating a crystal

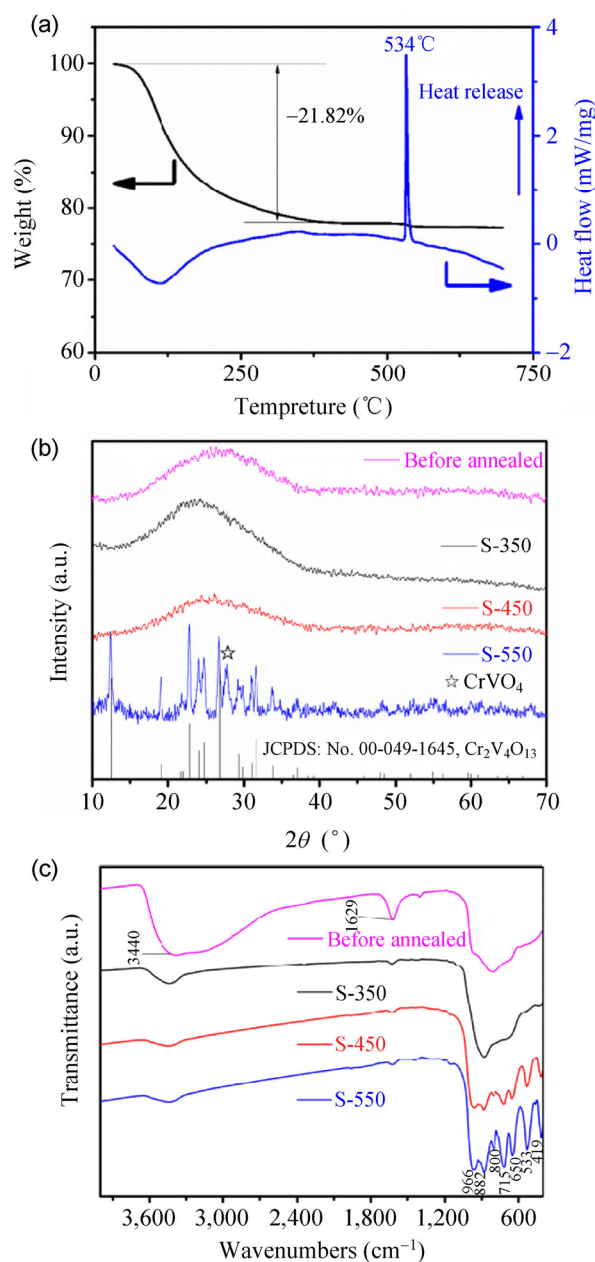


Figure 1 (a) TG analysis of Cr–V–O nanoparticles in air; XRD patterns (b) and FTIR spectra (c) of the products annealed at different temperatures.

structure transformation. To control the phase structure, temperature-dependent experiments were carried out. The precipitate precursors were annealed at 350 (denoted as S-350), 450 (denoted as S-450) and 550 °C (denoted as S-550) for 2 h in air with a rate of 2 °C/min. XRD was used to identify the crystallographic structure and crystallinity of the as-synthesized products, as shown in Fig. 1(b). There are no evident peaks in the XRD patterns of the samples annealed at 450 °C, which indicates the amorphous state of the products. After annealing at 550 °C, the sample becomes crystalline. Most of the diffraction peaks can be assigned to the monoclinic Cr₂V₄O₁₃ phase (JCPDS card No. 00-049-1645, $a = 8.287 \text{ \AA}$, $b = 9.300 \text{ \AA}$, $c = 7.530 \text{ \AA}$, $\beta = 109.17^\circ$). Some peaks ranging from 27.2° to 28.5° belong to CrVO₄ (JCPDS card No. 00-051-0031), indicating the presence of a mixed phase.

The TG curve (Fig. 1(a)) shows a large weight loss of the precursor which is related to the evaporation of the combined water, which can be confirmed by the endothermic peak (~100 °C) in the DSC curve. The weight loss is ~21.82%, which may correspond to the weight loss of the evaporation of the combined water in the Cr–V–O nanoparticles.

FTIR spectra (Fig. 1(c)) were obtained to confirm the covalent attachment of the entities in Cr–V–O samples prepared at different annealing temperatures. The bands at 3,440 and 1,629 cm⁻¹ correspond to O–H stretching and H–O–H bending modes [26], indicating the presence of bound water in the sample before annealing. With the increase of temperature, bands of bound water become weaker and other bands have become sharper, which represents the evaporation of the bound water and the crystallization process. The bands at 3,440 and 1,629 cm⁻¹ are still present after heat treatment, because some water was adsorbed during the testing process. It is interesting to note that there are no well-shaped absorption bands present in the spectrum of S-350, but sharp bands appear on increasing the annealing temperature (S-450 and S-550). These indicate that new chemical bonds have been formed in S-450, even though no peaks are evident in the XRD pattern. These results indicate that S-450 is in a state between amorphous and crystalline, and can be described as a metastable

amorphous state. The absorption bands with their maxima at 966 and 882 cm^{-1} correspond to the V–O stretching bond [34, 35]. Bands at 800 and 715 cm^{-1} correspond to the V–O–V stretching bond, and bands at 650, 533 and 419 cm^{-1} correspond to the Cr–O bond [35, 36]. These strong bands below 1,000 cm^{-1} further confirm the composition of the chromium–vanadium oxides.

The morphology and microstructure of the as-synthesized products before annealing were examined by FESEM (Fig. 2(a)). The nanoparticles are relatively monodisperse with a diameter of ~ 100 nm. After annealing at 450 °C (Fig. 2(b)), the nanoparticles do not change significantly. Energy dispersive X-ray spectroscopic element mapping analysis (Fig. 2(c)) indicates that Cr, V and O uniformly distributed in the nanoparticles. In addition, the EDS (Fig. S1 in the Electronic Supplementary Material (ESM)) of the nanoparticles exhibits strong Cr and V peaks. The atomic ratio of Cr and V is close to the expected 1:2 stoichiometry. SEM images of S-350 and S-550 are displayed in Fig. S2 (in the ESM). It is interesting to note that the nanoparticles become agglomerate due to the stress produced during the crystallization process, which indicates that further crystal structure transformation took place when the temperature reached 550 °C. The representative TEM images (Figs. 2(d) and 2(e)) show that the nanoparticles in S-450 are solid and ~ 100 nm in size. In the HRTEM

image (Fig. 2(f)) taken from an edge of a nanosized subunits, the absence of any clear lattice fringes further confirms its amorphous state, which is consistent with the XRD data.

However, TEM image of S-550 (Fig. S3(a), in the ESM) shows the agglomerate nanoparticles, which is consistent with the SEM image. Compared with the HRTEM image of S-450 (Fig. 2(e)), a clear lattice spacing of 3.32 Å is observed in the HRTEM image (Fig. S3(b)) of S-550, which matches well with the (012) plane of $\text{Cr}_2\text{V}_4\text{O}_{13}$.

XPS was used to elucidate the valence states of the ions present in S-450. The peaks corresponding to vanadium, oxygen, and chromium are seen in the survey-scan XPS for S-450 (Fig. 3(a)). The core binding energy for the Cr 2 $p_{3/2}$ peak (Fig. 3(b)) observed at ~ 576.9 eV agrees well with that of Cr^{3+} in chromium oxide [37]. The core binding energy for V 2 $p_{3/2}$ peak (Fig. 3(c)) observed at ~ 516.9 eV is in good agreement with that of V^{5+} in vanadium oxide [38]. The XPS data for other samples are displayed in Fig. S4 (in the ESM). The binding energies of Cr and V in S-350 and S-550 show little difference from those for S-450. The X-ray photoelectron spectra are consistent with the valence states of Cr and V in CrVO_4 and $\text{Cr}_2\text{V}_4\text{O}_{13}$, which further verifies the results above.

Coin cells with metallic lithium as the anode were assembled to investigate the electrochemical performance of the Cr–V–O nanoparticle cathodes. The cycling

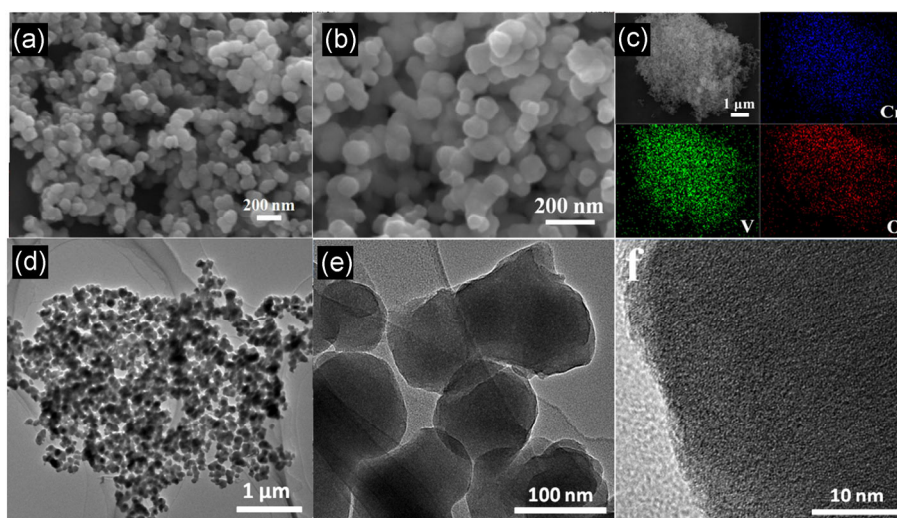


Figure 2 SEM images of the synthesized nanoparticles before annealing (a) and S-450 (b); EDS elemental mapping (c); TEM images (d) and (e) and HRTEM image (f) of S-450.

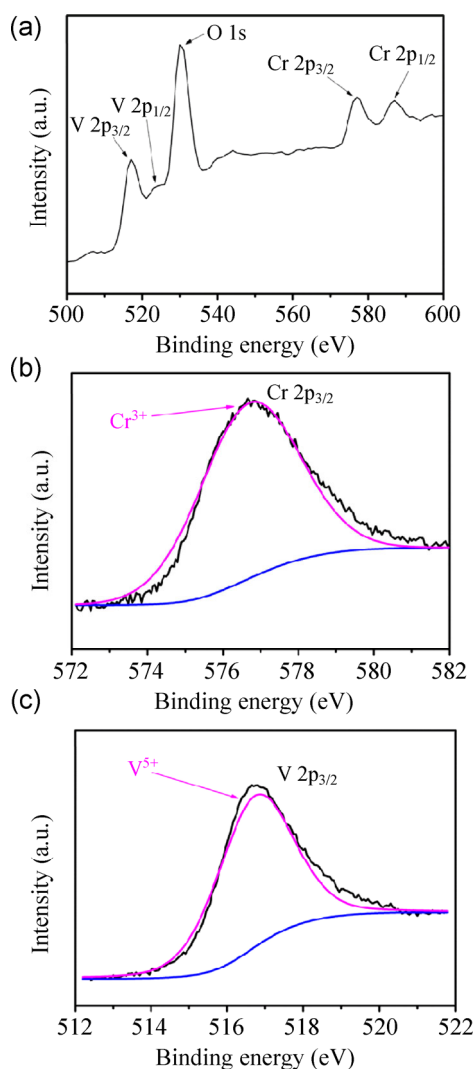


Figure 3 X-ray photoelectron spectra for the S-450 surface; (a) survey spectrum showing V (2p), O (1s) and Cr (2p) emanating from the sample; curve fitting for Cr 2p_{3/2} (b) and V 2p_{3/2} (c).

performance of the sample before annealing only exhibited a poor capacity of less than 25 mAh/g. (Fig. S5, in the ESM).

CVs of S-450 were measured at a scan rate of 0.1 mV/s in the potential range from 1.5 to 4.0 V (Fig. 4(a)). Only some smooth cathodic and anodic peaks can be observed in the CV curves, which indicates that the electrode host material forms a solid solution with Li [39]. In the subsequent scans, the shapes of the curves are almost identical, which indicates good reversibility of the lithium insertion/extraction process. Self-charge tests (Fig. S8(a), in the ESM) were carried out to further study the electrochemical mechanism. After being discharged to

1.5 V, the cell was rested for a long time, while the voltage was returned back to lower than 2 V. The result indicates that most of the Li ions were not separated from the cathode, demonstrating that the insertion/extraction reaction accounts for a major proportion, while the process is also accompanied by some absorbing/desorbing reactions. The SEM images (Fig. S6, in the ESM) of the cathode electrode prepared using S-450 are shown in Fig. S6 (in the ESM). Figures S6(a), S6(b) and S6(c) show the morphologies of the initial electrode, the electrode discharged to 1.5 V and the electrode charged to 4 V, respectively. There is no obvious difference in morphology between the three samples, which indicates that the structures of the material are well preserved. In addition, XPS measurements were recorded to characterize the electrode discharged to 1.5 V (Fig. S7, in the ESM). The result shows that all of chromium maintains the Cr³⁺ state, whilst much of the vanadium exhibits the V⁴⁺ state, indicating the occurrence of charge transfer in vanadium during the Li⁺ insertion process. The change of the vanadium valence state further demonstrates the insertion/extraction mechanism. Figure 4(b) displays the discharge/charge curves of all three Cr–V–O nanoparticle cathodes. These smooth sloping curves exhibit no obvious voltage plateau, which is consistent with the CV curves. To evaluate the rate capability, the samples were cycled at various rates, ranging from 100 to 3,000 mA/g (Fig. 4(c)). As the rate increases from 100 to 3,000 mA/g, the discharge capacity of S-450 decreases gradually from 260 to 85 mAh/g. After the high rate measurement, when the rate is reduced back to 100 mA/g, a discharge capacity of 250 mAh/g can be recovered, corresponding to 96.2% of the initial capacity. It is obvious that the capacity of S-450 is larger than that of S-350 and S-550 at both low and high current density. The cycling performance of S-450 was further evaluated by long-term galvanostatic discharge/charge testing. As shown in Fig. 4(d), an initial discharge capacity of 260 mAh/g at 100 mA/g is obtained. A capacity of 209 mAh/g is still retained after 200 cycles, corresponding to 80.4% of the initial capacity. Nitrogen adsorption–desorption isotherms (Fig. S8(b), in the ESM) were further measured to characterize the surface structure of S-450. The hysteresis loop shows

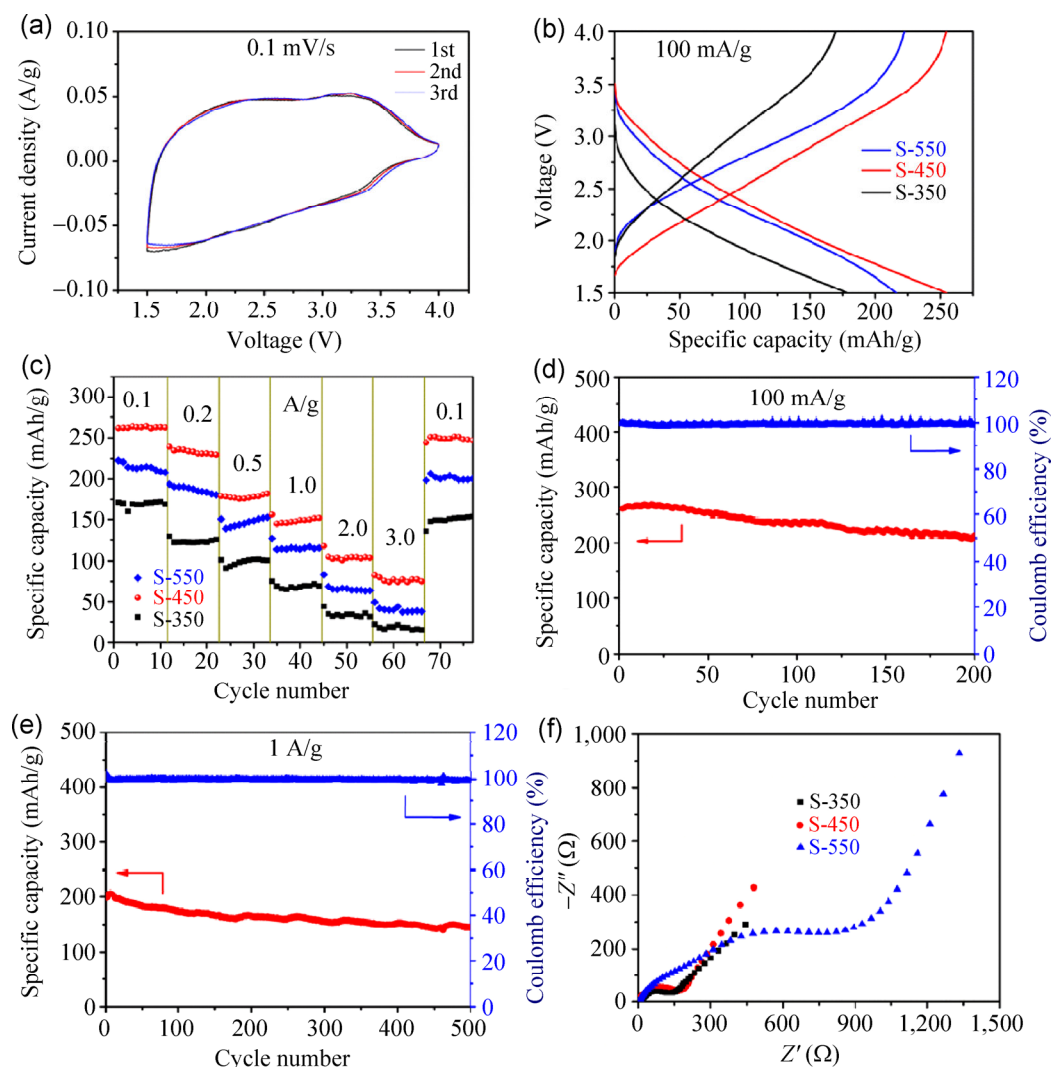


Figure 4 (a) Cyclic voltammograms at a scan rate of 0.1 mV/s of S-450; (b) discharge/charge curves of the second cycle at 100 mA/g of different samples; (c) the rate performance of samples annealed at different temperatures; (d) cycling performance of S-450 at the current density of 100 mA/g; (e) cycling performance of S-450 at a high rate of 1 A/g; (f) AC-impedance plots of products annealed at different temperatures.

that few mesopores exist in the material, and it is found that S-450 has a BET surface area of about $15 \text{ m}^2/\text{g}$, which cannot account for a capacity as high as 260 mAh/g . Thus involvement of the insertion/extraction mechanism is further confirmed. Although the capacity of Cr-V-O nanoparticles is lower than that of V_6O_{13} , the cycling stability of the metastable amorphous Cr-V-O nanoparticles is higher than that of lithiated V_6O_{13} nanosheets (94.8% vs. 69.2% capacity retained after 50 cycles) [40], and is also higher than Cr-modified V_6O_{13} (97.4% vs. 85.1% capacity retained after 35 cycles) [41]. The superior cycling stability of Cr-V-O nanoparticles is due to its particular

amorphous structure, which effectively prevents structure collapse during the insertion/extraction process of Li ions. Figure 4(e) shows the cycling performance at a high current density of 1 A/g. The initial discharge capacity of S-450 is 202 mAh/g , and the discharge capacity remains as high as 144 mAh/g after 500 cycles, corresponding to 71.3% of the initial capacity. During the cycling process, the coulomb efficiency remains around 100%. When tested in wider voltage ranges such as 1–4, 0.5–4 and 0–4 V, S-450 exhibits higher capacities (Fig. S9(a), in the ESM). From the cycling performance (Fig. S9(b)), we found that irrespective of the voltage range, the capacity

eventually stabilized at about 270 mAh/g, which may be the practical reversible capacity of S-450. The electrochemical impedance spectra (EIS) were also used to provide further insights (Fig. 4(f)). The frequency of the alternating current ranges from 0.01 Hz to 100 kHz, and the voltage is equal to the open circuit voltage of the cell at around 2.8 V. The Nyquist plots show the charge transfer resistance (R_{ct}) of S-350 and S-450 are much lower than that of the crystalline S-550, indicating that the amorphous state contributes much to the charge transfer.

The metastable amorphous S-450 exhibits better electrochemical performance than the other two samples. This can be attributed to several advantages of this metastable amorphous structure. Firstly, the disordered structure provides more active sites for Li^+ storage and wider channels than a crystalline material, and also avoids the collapse of a crystalline structure [33, 42], so S-450 possesses higher capacity than S-550. Secondly, the presence of a certain number of chemical bonds (Fig. 1(c)) in the metastable amorphous S-450 may improve the structure stability. Also the interspace in S-350 may be too large for Li^+ to be anchored, leading to the free movement of Li^+ in the material [43]. Thus the capacity and rate capability of S-450 are higher than those of S-350. The three structures are shown schematically in Fig. S10 (in the ESM). Thirdly, the presence of chromium ensures that the material maintains a low electrochemical impedance [28–30], which contributes significantly to the charge transfer. However, the voltage plateaus disappeared after addition of chromium, and we will conduct further studies of the reason for this. Furthermore, the nanostructures also afford drastically shortened diffusion distances for Li^+ .

4 Conclusions

A facile approach has been developed to prepare metastable amorphous Cr–V–O nanoparticles, by controlling the crystallization degree of the material. When evaluated as a cathode material for lithium batteries, it exhibits the highest electrochemical performance: Reversible capacity (260 mAh/g at 100 mA/g), low capacity loss (71.3% retained after 500 cycles at 1 A/g) and high rate capability (3 A/g). The enhanced

electrochemical performances result from the good diffusion channels for Li^+ , resulting from the particular metastable amorphous state with a certain amount of chemical bonds. Our results suggest that metastable amorphous Cr–V–O is a promising material for lithium storage.

Acknowledgements

This work is supported by the National Basic Research Program of China (Nos. 2013CB934103 and 2012CB933003), the National Natural Science Foundation of China (Nos. 51272197 and 51302203), the National Science Fund for Distinguished Young Scholars of China, the International Science and Technology Cooperation Program of China (No. 2013DFA50840) and the Fundamental Research Funds for the Central Universities (Nos. 2013-ZD-7, 2013-IV-131, and 2014-VII-007). We are grateful to Prof. C. M. Lieber of Harvard University and Prof. D. Y. Zhao of Fudan University for strong support and stimulating discussions. The authors declare no competing financial interest. All authors discussed the results and commented on the manuscript.

Electronic Supplementary Material: Supplementary material (EDS of S-450, SEM images of S-350 and S-550, TEM and HRTEM images of S-550, cycling performance at the current density of 100 mA/g of the nanoparticles before annealing, crystal structures of the amorphous, metastable amorphous and crystalline states) is available in the online version of this article at <http://dx.doi.org/10.1007/s12274-014-0520-1>.

References

- [1] Kang, B.; Ceder, G. Battery materials for ultrafast charging and discharging. *Nature* **2009**, *458*, 190–193.
- [2] Goodenough, J. B.; Kim, Y. Challenges for rechargeable Li batteries. *Chem. Mater.* **2009**, *22*, 587–603.
- [3] Kang, K.; Meng, Y. S.; Bréger, J.; Grey, C. P.; Ceder, G. Electrodes with high power and high capacity for rechargeable lithium batteries. *Science* **2006**, *311*, 977–980.
- [4] Liu, J. P.; Jiang, J.; Cheng, C. W.; Li, H. X.; Zhang, J. X.; Gong, H.; Fan, H. J. Co_3O_4 nanowire@ MnO_2 ultrathin nanosheet core/shell arrays: A new class of high-performance pseudocapacitive materials. *Adv. Mater.* **2011**, *23*, 2076–2081.

- [5] Hassoun, J.; Reale, P.; Scrosati, B. Recent advances in liquid and polymer lithium-ion batteries. *J. Mater. Chem.* **2007**, *17*, 3668–3677.
- [6] Li, L.; Zhai, T. Y.; Bando, Y.; Golberg, D. Recent progress of one-dimensional ZnO nanostructured solar cells. *Nano Energy* **2012**, *1*, 91–106.
- [7] Tarascon, J. M.; Armand, M. Issues and challenges facing rechargeable lithium batteries. *Nature* **2001**, *414*, 359–367.
- [8] Wang, L.; He, X. M.; Sun, W. T.; Wang, J. L.; Li, Y. D.; Fan, S. S. Crystal orientation tuning of LiFePO₄ nanoplates for high rate lithium battery cathode materials. *Nano Lett.* **2012**, *12*, 5632–5636.
- [9] Mai, L. Q.; Wei, Q. L.; An, Q. Y.; Tian, X. C.; Zhao, Y. L.; Xu, X.; Xu, L.; Chang, L.; Zhang, Q. J. Nanoscroll buffered hybrid nanostructural VO₂ (B) cathodes for high-rate and long-life lithium storage. *Adv. Mater.* **2013**, *25*, 2969–2973.
- [10] Simon, P.; Gogotsi, Y. Materials for electrochemical capacitors. *Nat. Mater.* **2008**, *7*, 845–854.
- [11] Cao, Y. L.; Li, X. L.; Aksay, I. A.; Lemmon, J.; Nie, Z. M.; Yang, Z. G.; Liu, J. Sandwich-type functionalized graphene sheet–sulfur nanocomposite for rechargeable lithium batteries. *Phys. Chem. Chem. Phys.* **2011**, *13*, 7660–7665.
- [12] Whittingham, M. S. Lithium batteries and cathode materials. *Chem. Rev.* **2004**, *104*, 4271–4302.
- [13] Xiao, X. L.; Yang, L. M.; Zhao, H.; Hu, Z. B.; Li, Y. D. Facile synthesis of LiCoO₂ nanowires with high electrochemical performance. *Nano Res.* **2012**, *5*, 27–32.
- [14] Liu, J.; Xia, H.; Xue, D. F.; Lu, L. Double-shelled nanocapsules of V₂O₅-based composites as high-performance anode and cathode materials for Li ion batteries. *J. Am. Chem. Soc.* **2009**, *131*, 12086–12087.
- [15] Kannan, A.; Rabenberg, L.; Manthiram, A. High capacity surface-modified LiCoO₂ cathodes for lithium-ion batteries. *Electrochem. Solid-State Lett.* **2003**, *6*, A16–A18.
- [16] Madhavi, S.; Subba Rao, G.; Chowdari, B.; Li, S. F. Y. Effect of Cr dopant on the cathodic behavior of LiCoO₂. *Electrochim. Acta* **2002**, *48*, 219–226.
- [17] Nan, C. Y.; Lu, J.; Li, L. H.; Li, L. L.; Peng, Q.; Li, Y. D. Size and shape control of LiFePO₄ nanocrystals for better lithium ion battery cathode materials. *Nano Res.* **2013**, *6*, 469–477.
- [18] Zhang, W. J. Structure and performance of LiFePO₄ cathode materials: A review. *J. Power Sources* **2011**, *196*, 2962–2970.
- [19] An, Q. Y.; Zhang, P. F.; Wei, Q. L.; He, L.; Xiong, F. Y.; Sheng, J. Z.; Wang, Q. Q.; Mai, L. Q. Top-down fabrication of three-dimensional porous V₂O₅ hierarchical microplates with tunable porosity for improved lithium battery performance. *J. Mater. Chem. A* **2014**, *2*, 3297–3302.
- [20] Zhang, C. F.; Chen, Z. X.; Guo, Z. P.; Lou, X. W. Additive-free synthesis of 3D porous V₂O₅ hierarchical microspheres with enhanced lithium storage properties. *Energ. Environ. Sci.* **2013**, *6*, 974–978.
- [21] Sathiya, M.; Prakash, A.; Ramesha, K.; Tarascon, J. M.; Shukla, A. K. V₂O₅-anchored carbon nanotubes for enhanced electrochemical energy storage. *J. Am. Chem. Soc.* **2011**, *133*, 16291–16299.
- [22] Mai, L. Q.; Dong, Y. J.; Xu, L.; Han, C. H. Single nanowire electrochemical devices. *Nano Lett.* **2010**, *10*, 4273–4278.
- [23] Hu, B.; Zhang, Y.; Chen, W.; Xu, C.; Wang, Z. L. Self-heating and external strain coupling induced phase transition of VO₂ nanobeam as single domain switch. *Adv. Mater.* **2011**, *23*, 3536–3541.
- [24] Kaveevivitchai, W.; Jacobson, A. J. High capacity microporous molybdenum–vanadium oxide electrodes for rechargeable lithium batteries. *Chem. Mater.* **2013**, *25*, 2708–2715.
- [25] Cheng, F. Y.; Chen, J. Transition metal vanadium oxides and vanadate materials for lithium batteries. *J. Mater. Chem.* **2011**, *21*, 9841–9848.
- [26] Mai, L. Q.; Xu, L.; Han, C. H.; Xu, X.; Luo, Y. Z.; Zhao, S. Y.; Zhao, Y. L. Electrospun ultralong hierarchical vanadium oxide nanowires with high performance for lithium ion batteries. *Nano Lett.* **2010**, *10*, 4750–4755.
- [27] Xu, H. H.; Shu, J.; Hu, X. L.; Sun, Y. M.; Luo, W.; Huang, Y. H. Electrospun porous LiNb₃O₈ nanofibers with enhanced lithium-storage properties. *J. Mater. Chem. A* **2013**, *1*, 15053–15059.
- [28] Shi, S. Q.; Liu, L. J.; Ouyang, C. Y.; Wang, D. S.; Wang, Z. X.; Chen, L. Q.; Huang, X. J. Enhancement of electronic conductivity of LiFePO₄ by Cr doping and its identification by first-principles calculations. *Phys. Rev. B* **2003**, *68*, 195108.
- [29] Ouyang, C. Y.; Shi, S. Q.; Wang, Z. X.; Li, H.; Huang, X. J.; Chen, L. Q. The effect of Cr doping on Li ion diffusion in LiFePO₄ from first principles investigations and Monte Carlo simulations. *J. Phys.: Condens. Mat.* **2004**, *16*, 2265–2272.
- [30] Park, S. B.; Eom, W. S.; Cho, W. I.; Jang, H. Electrochemical properties of LiNi_{0.5}Mn_{1.5}O₄ cathode after Cr doping. *J. Power Sources* **2006**, *159*, 679–684.
- [31] Leger, C.; Bach, S.; Soudan, P.; Pereira-Ramos, J. P. Evaluation of the sol–gel mixed oxide Cr_{0.11}V₂O_{5.16} as a rechargeable positive electrode working in the potential range 3.8/1.5 V vs. Li. *Solid State Ionics* **2005**, *176*, 1365–1369.
- [32] Lee, J.; Urban, A.; Li, X.; Su, D.; Hautier, G.; Ceder, G. Unlocking the potential of cation-disordered oxides for rechargeable lithium batteries. *Science* **2014**, *343*, 519–522.

- [33] Hibino, M.; Abe, K.; Mochizuki, M.; Miyayama, M. Amorphous titanium oxide electrode for high-rate discharge and charge. *J. Power Sources* **2004**, *126*, 139–143.
- [34] Šurca, A.; Orel, B. IR spectroscopy of crystalline V_2O_5 films in different stages of lithiation. *Electrochim. Acta* **1999**, *44*, 3051–3057.
- [35] Filipek, E.; Walczak, J.; Tabero, P. Synthesis and some properties of the phase $Cr_2V_4O_{13}$. *J. Alloy. Compd.* **1998**, *265*, 121–124.
- [36] Musić, S.; Maljković, M.; Popović, S.; Trojko, R. Formation of chromia from amorphous chromium hydroxide. *Croat. Chem. Acta* **1999**, *72*, 789–802.
- [37] Marcus, P.; Grimal, J. M. The anodic dissolution and passivation of Ni–Cr–Fe alloys studied by ESCA. *Corros. Sci.* **1992**, *33*, 805–814.
- [38] Hopfengärtner, G.; Borgmann, D.; Rademacher, I.; Wedler, G.; Hums, E.; Spitznagel, G. XPS studies of oxidic model catalysts: Internal standards and oxidation numbers. *J. Electron Spectrosc. Relat. Phenom.* **1993**, *63*, 91–116.
- [39] Van der Ven, A.; Bhattacharya, J.; Belak, A. A. Understanding Li diffusion in Li-Intercalation compounds. *Acc. Chem. Res.* **2012**, *46*, 1216.
- [40] Tian, X. C.; Xu, X.; He, L.; Wei, Q. L.; Yan, M. Y.; Xu, L.; Zhao, Y. L.; Yang, C. C.; Mai, L. Q. Ultrathin pre-lithiated V_6O_{13} nanosheet cathodes with enhanced electrical transport and cyclability. *J. Power Sources* **2014**, *255*, 235–241.
- [41] Leger, C.; Bach, S.; Pereira-Ramos, J. The sol–gel chromium-modified V_6O_{13} as a cathodic material for lithium batteries. *J. Solid State Electrochem.* **2007**, *11*, 71–76.
- [42] Okada, S.; Yamamoto, T.; Okazaki, Y.; Yamaki, J. I.; Tokunaga, M.; Nishida, T. Cathode properties of amorphous and crystalline $FePO_4$. *J. Power Sources* **2005**, *146*, 570–574.
- [43] Chen, L.; Gu, Q. W.; Zhou, X. F.; Lee, S.; Xia, Y. G.; Liu, Z. P. New-concept batteries based on aqueous Li^+/Na^+ mixed-ion electrolytes. *Sci. Rep.* **2013**, *3*, 1946.